ScieRxiv

NOT PEER-REVIEWED

Research Article

Hierarchical architectures in Cr-doped $GdTaO_4$ for boosted high-temperature thermal protection performance

Manyu Zhang[1], Binbin Wu[2], Mingzhu Peng[1], Jun Wang[1]*, Jinwen Yang[1], Ronghai Liu[3], Hanyu Li[3], Fangcheng Qiu[3], Peng Wu[1], Zhenhua Ge[1], Jing Feng[1]*

[1]Faculty of Materials Science and Engineering, Kunming University of Science and Technology, Kunming 650093, Yunnan, China.

[2]Shanghai KoKo Valve Group Co., Ltd., Shanghai, 201802, China.

[3]Electric Power Research Institute of Yunnan Power Grid Co, Ltd, Kunming, 650217, Yunnan, China.

Received: 17 June 2026 | Approved: 02 July 2026 | Online: 02 July 2026

Abstract

The main purpose of thermal protection materials is to minimise heat conduction toward the substrate interior through low thermal conductivity and enhanced heat radiation to the external environment via high emissivity. Herein, novel thermal barrier ceramic materials based on $(Gd_{1-x}Cr_x)TaO_4$ with high emissivity and low thermal conductivity were synthesized via a solid-phase method. $(Gd_{0.95}Cr_{0.05})TaO_4$ exhibited the lowest intrinsic thermal conductivity of 1.03 $W \cdot m^{-1} \cdot K^{-1}$ at 1,600°C and the highest emissivity of 0.81 across a 1-14 μm wavelength range at 800 °C, which both enhanced its thermal insulation performance. The low intrinsic thermal conductivity of $(Gd_{0.95}Cr_{0.05})TaO_4$ originated from hierarchical architectures defect phonon scattering, including point defects, dislocations, domain boundaries and grain boundaries. Furthermore, Cr^{3+}

© The Author(s) 2026. Open Access This article is licensed under a Creative Commons Attribution 4.0 International License (https://creativecommons.org/licenses/by/4.0/), which permits unrestricted use, sharing, adaptation, distribution and reproduction in any medium or format, for any purpose, even commercially, as long as you give appropriate credit to the original author(s) and the source, provide a link to the Creative Commons license, and indicate if changes were made.

doping increased the radiative thermal conductivity while enhancing phonon scattering and phonon-photon coupling effects. The high emissivity of $(Gd_{0.95}Cr_{0.05})TaO_4$ was dominated by high free carrier absorption and vibrational absorption. Moreover, the introduction of Cr^{3+} induced *d-d* electron transitions and generated new absorption bands in the infrared region, thus enhancing thermal radiation. These results indicate that $(Gd_{0.95}Cr_{0.05})TaO_4$ is a promising candidate for use as an innovative thermal protection coating material at elevated temperatures.

Keywords: Thermal barrier coating (TBC), thermal conductivity, emissivity, hierarchical architectures, rare earth tantalates

INTRODUCTION

The primary function of thermal protection materials[1,2] is to reduce heat conduction toward the substrate interior through low thermal conductivity and enhance heat radiation to the external environment via high emissivity, thereby effectively lowering the substrate temperature. Thermal protection materials have a wide range of applications in both military and civilian fields, including high-temperature hot-end components in space exploration, aerospace, nuclear power engineering, gas turbines and industrial energy conservation[3,4].

Currently, the primary high-temperature thermal protection materials mainly consist of transition metal oxides (A_2O_3)[5], oxide spinels (AB_2O_4)[6] and perovskites (ABO_3)[7]. Other thermal barrier ceramic coating materials include $RE_2Zr_2O_7$[8], $RE_2Si_2O_7$[9], $RESi_2O_5$[10], $RE_4Al_2O_9$[11], $RE_2Ce_2O_7$[12], $RENbO_4$[13] and $RETaO_4$[14]. Among these, rare earth tantalates ($RETaO_4$) have emerged as leading candidate materials for extreme environments (> 1,600 °C) due to their exceptionally low thermal conductivity, outstanding high-temperature phase stability, superior sintering resistance and ferroelastic domain toughening[15-17], especially $GdTaO_4$[18]. However, most research has so far focused on the low thermal conductivity of $RETaO_4$[19], with its thermal radiation properties remaining unreported. Therefore, there is an urgent need to develop

integrated $RETaO_4$ materials with low thermal conductivity and high emissivity by tuning their hierarchical architectures.

Doping strategies are an effective approach to improving the emissivity of these thermal protection materials. The process involves introducing gap states and lattice distortions into the host structure[20]. Doping with RE^{3+} ions increases phonon vibration absorption in the long-wavelength band, while doping with transition metal cations (such as Cr^{3+}, Mn^{4+}, Fe^{4+} and Ti^{4+}) contributes to enhancing phonon vibration absorption in the near-infrared band[21-23]. Regarding the modification of emission efficiency through RE doping, Huang *et al.*[24] employed Electron beam physical vapor deposition (EB-PVD) to fabricate CeO_2 coatings doped with La^{3+} at varying molar ratios onto nickel-based high-temperature alloy substrates. The emissivity of these coatings across the long-wave infrared range of 2.5-25 μm at 600, 800 and 1,000 °C increased with increasing La^{3+} doping levels. In terms of transition metal doping to modify the emissivity, Ma *et al.*[25] reported that partially substituting Zr^{4+} with Ti^{4+} in $Sm_2Zr_2O_7$ further enhanced the infrared emissivity in the near-infrared band. Similarly, Meng *et al.*[20] employed a solid-state reaction method to synthesize $LaCr_{1-x}Mg_xO_3$, with the results indicating that the near-infrared emission at 2.5-5.0 μm significantly increased with Mg^{2+} doping. This enhanced emission was primarily attributed to the increased oxygen vacancies and reduced band gap, which facilitated electron transitions and free carrier absorption, thereby enhancing its near-infrared radioactive properties.

Herein, $(Gd_{1-x}Cr_x)TaO_4$ ceramics with high emissivity and low thermal conductivity are synthesized via a solid-phase method. A systematic investigation is conducted on their microstructure, defect formation mechanism and origin of low thermal conductivity and high emissivity. Their mechanical properties, including modulus and hardness, are also studied. Furthermore, the thermal protection performance of $(Gd_{1-x}Cr_x)TaO_4$ is compared with traditional coating materials, namely, 8YSZ and $La_2Zr_2O_7$. Using dynamic thermal insulation performance test, we demonstrated that $(Gd_{0.95}Cr_{0.05})TaO_4$ with low thermal conductivity and high emissivity exhibited a greater temperature

gradient, indicating that it holds promise as a novel thermal protection coating material for high temperatures.

EXPERMENTAL

Materials synthesis

The raw materials for synthesizing $(Gd_{1-x}Cr_x)TaO_4$ include gadolinium oxide (Gd_2O_3), tantalum oxide (Ta_2O_5) and chromium oxide (Cr_2O_3) (> 99.9%, Shanghai Aladdin Bio-Chem Technology Co., Ltd., China). $(Gd_{1-x}Cr_x)TaO_4$ (x = 0, 5, 10, 15 and 20) ceramics were synthesized using a solid-state reaction method. The raw powder was weighed according to the stoichiometric ratio, placed in a ball mill with anhydrous ethanol as the solvent and ground for 12 h at 350 rpm. Afterward, the mixture was dried in a drying oven at 80 °C and the dried powder was sieved through a 300-mesh screen to remove coarse agglomerates. The sieved powder was uniaxially pressed to form disk-shaped bulks with a diameter of 15 mm at 10 MPa for 3 min. The pressed bulks were further densified by cold isostatic pressing at 600 MPa for 5 min, followed by sintering at 1,700 °C for 10 h.

Characterization

X-ray diffraction (XRD; MiniFlex-600; Rigaku, city, Japan) was used to characterize the phase structure with a scanning angle of 10-80° at 2°/min. The microstructural morphology was observed using field emission scanning electron microscopy (SEM; JSM-7001 F; city, Japan) and high-angle annual dark field-scanning translation electron microscopy (HAADF-STEM; JEM-ARM 200F; NEOARM, city, Japan). Scanning electron microscopy equipped with energy-dispersive X-ray spectroscopy (EDS; company, Oxford, UK) was employed to analyze the elemental distribution of the ceramics. An IR-VASE ellipsometer (IR-VASE; J. A., city, state, USA) was used to analyze the extinction coefficient and refractive index of the ceramics.

The transverse wave (v_t) and longitudinal wave (v_l) sound velocities were measured using an Advanced Ultrasonic Modulus measurement system (UMS-100; TECLAB,

Chelles, France) under ambient conditions. The mean acoustic velocity (v_m), Poisson ratio (σ), Young's modulus (E), shear modulus (G), bulk modulus (B), Grüneisen parameter (γ) and Debye temperature (θ_D) were determined using the following formulae[26]:

$$v_m=\left[\frac{1}{3}\left(\frac{1}{v_l^3}+\frac{2}{v_t^3}\right)\right]^{-\frac{1}{3}} \quad (1)$$

$$\sigma=\frac{1-2(v_t/v_l)^2}{2-2(v_t/v_l)^2} \quad (2)$$

$$E=\frac{\rho v_t^2(3v_l^2-4v_t^2)}{v_l^2-v_t^2} \quad (3)$$

$$G=\frac{E}{2(2+\sigma)} \quad (4)$$

$$B=\rho\left(v_l^2-\frac{4}{3}v_t^2\right) \quad (5)$$

$$\gamma=\frac{3}{2}\left(\frac{1+\sigma}{2-3\sigma}\right) \quad (6)$$

$$\theta_D=\frac{h}{k_B}\left(\frac{3N}{4\pi V}\right)^{\frac{1}{3}}\times v_m \quad (7)$$

where the constants h and k_B correspond to Planck's constant and the Boltzmann constant, respectively, N represents the number of atoms within a unit cell, and V denotes the volume of the unit cell. Moreover, the nanoscale hardness and Young's modulus of $(Gd_{1-x}Cr_x)TaO_4$ were investigated using the nanoindentation technique with a NanoBlitz 3D instrument (G200; Agilent, city, state, USA).

The thermal diffusivity (α) of the samples was measured from 25 to 1,600 °C utilizing a laser flash apparatus (Netzsch LFA 427; company, Bavaria, Germany). Subsequently, the thermal conductivity (κ) was calculated based on the following formula[27]:

$$\kappa=\rho C_p \alpha \quad (8)$$

where ρ (density) was measured via the Archimedes method and C_p (specific heat capacity per unit mass) was derived from the Neumann-Kopp rule. The corrected actual thermal conductivity (κ') for dense samples was calculated based on the following formula[28]:

$$\kappa'=\kappa/(1-4\varphi/3) \quad (9)$$

where φ is the porosity. Moreover, the thermal expansion properties were ascertained by means of a thermomechanical analyzer (TMA-402 F3; Netzsch, city, Germany).

The emissivity spectra of the ceramic materials were recorded over the 1-14 μm spectral region at 800 °C via the energy comparison approach, (The emissivity data were acquired utilizing a high-temperature measurement platform independently established by the Harbin Institute of Technology, China) as described by the equation below[29]:

$$\varepsilon=\frac{E_g}{E_b} \quad (10)$$

where E_g (W/m^2) is the radiation energy emitted from the object and E_b (W/m^2) is the radiation energy emitted from the calibrated blackbody at 800 °C. Additionally, the average emissivity ($\bar{\varepsilon}$) in the range from λ_1 to λ_2 wavelength is calculated by the ratio of the total energy emitted for the sample to the total energy emitted for the blackbody based on the following formula:

$$\bar{\varepsilon}=\frac{\int_{\lambda_1}^{\lambda_2}\varepsilon(\lambda)\frac{C_1\lambda^{-5}}{e^{\frac{C_2}{\lambda T}}-1}d\lambda}{\int_{\lambda_1}^{\lambda_2}\frac{C_1\lambda^{-5}}{e^{\frac{C_2}{\lambda T}}-1}d\lambda} \quad (11)$$

where ε denotes the spectral emissivity at wavelength λ (μm), and C_1 and C_2 are the first and second radiation constants, taking values of 3.742 × 108 W/(μm^4· m^2) and 14,387.9 μm· K, respectively. The symbol $\bar{\varepsilon}$ represents the average emissivity calculated over a specified wavelength interval.

First-principles calculations

First-principles calculations based on density functional theory (DFT) were carried out using the Vienna Ab Initio Simulation Package (VASP)[30] within the projector augmented wave (PAW) formalism[31]. The exchange-correlation energy was described by the Perdew-Burke-Ernzerhof (PBE) functional under the generalized gradient approximation (GGA)[32], and spin polarization was not taken into account. A plane-wave basis set with a cutoff energy of 400 eV was employed, along with 2×1×2 supercells for $(Gd_{1-x}Cr_x)TaO_4$. Sampling of the Brillouin zone was conducted using the Monkhorst-Pack scheme with a uniform grid spacing of 0.04 Å.

RESULTS

Superior thermal protection performance

The main function of radiative thermal protection coatings is reducing the substrate temperature by efficiently dissipating heat through radiation and limiting heat conduction into the substrate. Materials as radiative thermal protection coatings required low thermal conductivity to effectively block heat transfer to the substrate and high emissivity to enhance radiative heat dissipation. Key thermal transfer performance indicators, comprising emissivity and thermal conductivity, were compared between $(Gd_{0.95}Cr_{0.05})TaO_4$ and other typical thermal protection materials[29,33-37] as shown in Figure 1(a). The results demonstrated that $(Gd_{0.95}Cr_{0.05})TaO_4$ exhibited both a low experimental thermal conductivity (1.03 W·m^{-1}·K^{-1}) and a high emissivity (0.81), thereby enhancing its thermal protection performance. To further assess the thermal insulation performance of bulk $(Gd_{0.95}Cr_{0.05})TaO_4$, we compared its temperature drop gradients with conventional thermal barrier coatings, 8YSZ and bulk $La_2Zr_2O_7$, with a thickness of 1.5 mm using a thermal insulation testing system, as shown in Figure 1(b).

The back surface temperature of $(Gd_{0.95}Cr_{0.05})TaO_4$ at 785 °C was significantly lower than that of 8YSZ at 968 °C and $La_2Zr_2O_7$ at 835 °C under identical conditions (1,350 °C for 32s), indicating that $(Gd_{0.95}Cr_{0.05})TaO_4$ possessed greater temperature drop gradients (565 °C) and superior thermal insulation performance. These results arose from the low thermal conductivity and high emissivity of $(Gd_{0.95}Cr_{0.05})TaO_4$. The former inhibited the thermal conduction rate, while the latter enhanced surface radiative thermal dissipation, and the synergistic effect co-enhanced the thermal insulation performance for $(Gd_{0.95}Cr_{0.05})TaO_4$.

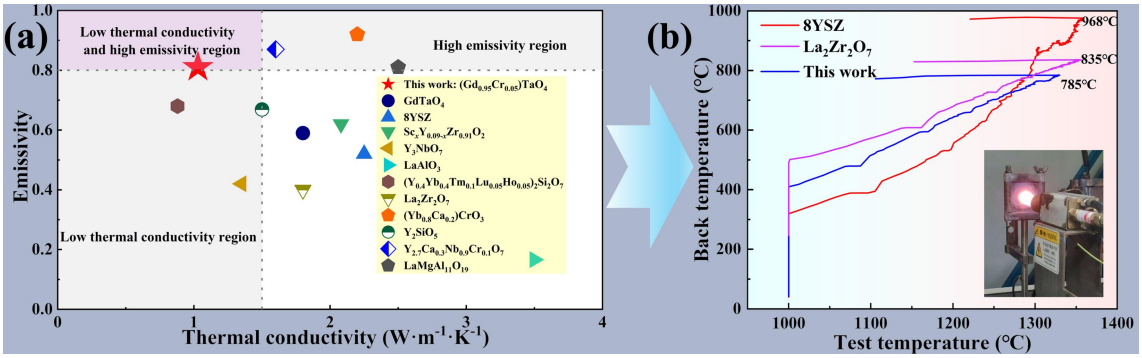

Figure 1. Thermal protection properties. (a) emissivity and thermal conductivity of $(Gd_{0.95}Cr_{0.05})TaO_4$ compared with other traditional materials; (b) dynamic thermal insulation performance test conducted on bulk $(Gd_{0.95}Cr_{0.05})TaO_4$, 8YSZ, and $La_2Zr_2O_7$ specimens at 1,350 °C.

Phase stability and structural characterization

Figure 2(a) shows the XRD patterns of the $(Gd_{1-x}Cr_x)TaO_4$ samples. The diffraction peaks of the samples matched with the standard card (PDF#24-0441) of $GdTaO_4$, indicating that $(Gd_{1-x}Cr_x)TaO_4$ with a monoclinic (*m* phase) structure was successfully synthesized. Additionally, the XRD refinement results are shown in Figure 2(b-f). Both the weighted pattern variance factor (R_{wp}) and pattern variance factor (R_p) were less than 5%, indicating that the refinement results were highly reliable. Table 1 summarizes the lattice parameters (*a*, *b*, and *c*), theoretical density (ρ_{cal}), and unit cell volume (*V*) obtained from Rietveld refinement.

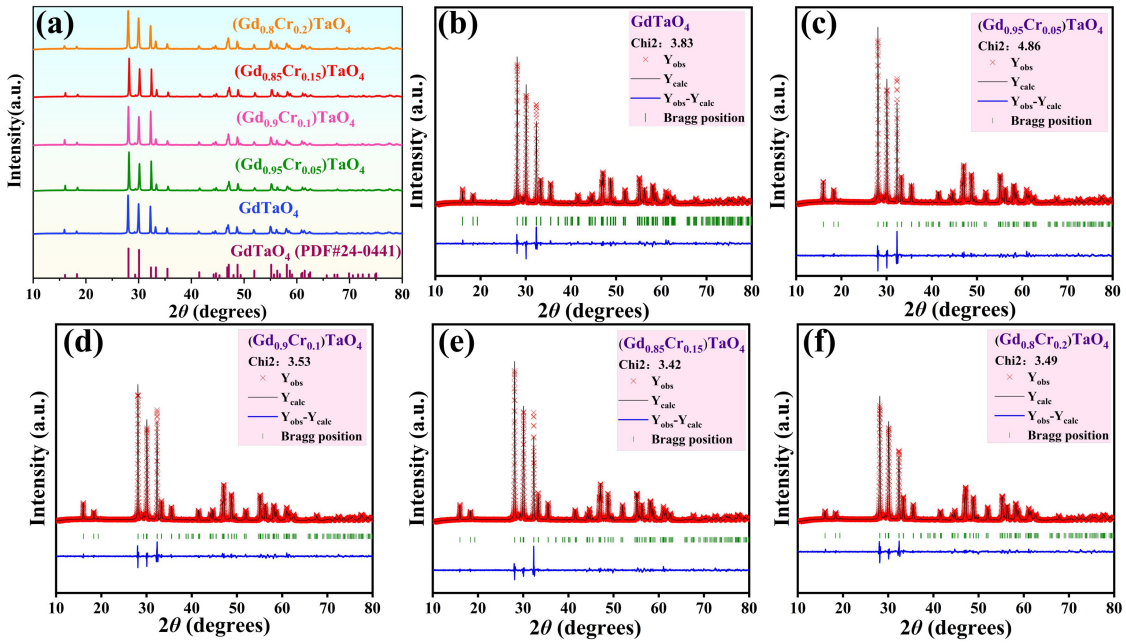

Figure 2. Phase structural characterization of $(Gd_{1-x}Cr_x)TaO_4$. (a) XRD patterns; (b-f) refined XRD patterns.

Table 1. Lattice parameters (*a*, *b* and *c*), unit cell volumes (*V*) and theoretical densities (*ρ*) of $(Gd_{1-x}Cr_x)TaO_4$.

Sample	*a* (Å)	*b* (Å)	*c* (Å)	*V* (Å^3)	*ρ* (g·cm^{-3})
$GdTaO_4$	5.407	11.072	5.081	302.711	8.83
$(Gd_{0.95}Cr_{0.05})TaO_4$	5.407	11.075	5.079	302.682	8.71
$(Gd_{0.9}Cr_{0.1})TaO_4$	5.405	11.072	5.077	302.399	8.60
$(Gd_{0.85}Cr_{0.15})TaO_4$	5.402	11.071	5.080	302.355	8.49
$(Gd_{0.8}Cr_{0.2})TaO_4$	5.398	11.060	5.074	301.530	8.40

To evaluate the influence of Cr^{3+} incorporation on the degree of lattice distortion, the distortion parameter (Δd) was calculated using the following expression[28]:

$$\Delta d = \frac{1}{n}\sum_{i=1}^{n}\left[\frac{d(\mathrm{RE/Ta\text{-}O})_i - \overline{d(\mathrm{RE/Ta\text{-}O})}}{\overline{d(\mathrm{RE/Ta\text{-}O})}}\right]^2 \quad (12)$$

where $d(\mathrm{RE/Ta{-}O})_i$ is the bond length of RE−O or Ta−O for the ith O atom and

$\overline{d(\text{RE/Ta-O})}$ is their average bond length. Table 2 shows the total distortion degree Δd of $(Gd_{1-x}Cr_x)TaO_4$, indicating that the introduction of Cr^{3+} led to increased distortion.

Table 2. Bond lengths (Ta-O and RE-O (Å)) and distortion degrees (Δd_{tot} (%)) of $(Gd_{1-x}Cr_x)TaO_4$.

Samples	Bond	Bond length (l/Å)				Average bond length (l/Å)	Δd (%)	Δd_{tot} (%)
$GdTaO_4$	Ta-O	1.913	1.826	---	---	1.869	0.055	0.222
	Gd-O	2.528	2.509	2.346	2.301	2.421	0.168	
$(Gd_{0.95}Cr_{0.05})TaO_4$	Ta-O	1.849	1.931	2.428	---	2.069	1.527	1.553
	RE-O	2.380	2.443	2.337	2.400	2.390	0.025	
$(Gd_{0.9}Cr_{0.1})TaO_4$	Ta-O	1.898	1.924	2.318	---	2.047	0.881	0.951
	RE-O	2.344	2.379	2.392	2.513	2.047	0.070	
$(Gd_{0.85}Cr_{0.15})TaO_4$	Ta-O	1.807	1.872	2.318	---	1.999	1.291	1.559
	RE-O	2.558	2.285	2.383	2.596	2.456	0.268	
$(Gd_{0.8}Cr_{0.2})TaO_4$	Ta-O	2.017	1.907	2.336	---	2.087	0.760	1.200
	RE-O	2.250	2.217	2.338	2.614	2.355	0.439	

Mechanical properties

The transverse and longitudinal sound velocities were measured using the ultrasonic pulse method for the samples, as shown in Table 3.The ductility of the materials can be estimated by the ratio of shear modulus to bulk modulus (G/B)[38]. When G/B was less than 0.57, the materials were brittle and vice versa for ductile materials. The G/B values for $(Gd_{1-x}Cr_x)TaO_4$ were 0.37, 0.37, 0.40, 0.29 and 0.33, respectively, all of which were less than 0.57, indicating that $(Gd_{1-x}Cr_x)TaO_4$ was a brittle material.

Table 3. Transverse acoustic velocity (v_t), longitudinal acoustic velocity (v_l), mean acoustic velocity (v_m), Poisson's ratio (σ), Young's modulus (E), bulk modulus (B),

shear modulus (G), Grüneisen parameter (γ) and Debye temperature (θ_D) of $(Gd_{1-x}Cr_x)TaO_4$.

Sample	υ_t	υ_l	υ_m	σ	E	B	G	γ	θ_D
$GdTaO_4$	2,414	4,856	2,709	0.34	131	133	49	2.02	349
$(Gd_{0.95}Cr_{0.05})TaO_4$	2,656	5,346	2,981	0.34	159	162	60	2.02	387
$(Gd_{0.9}Cr_{0.1})TaO_4$	2,418	4,727	2,909	0.32	129	122	49	1.92	349
$(Gd_{0.85}Cr_{0.15})TaO_4$	2,428	5,310	2,737	0.37	135	170	49	2.29	355
$(Gd_{0.8}Cr_{0.2})TaO_4$	2,566	5,369	2,886	0.35	149	168	55	2.15	372

Figures 3(a-e) show the Young's modulus of $(Gd_{1-x}Cr_x)TaO_4$ measured by the nanoindentation technique, with the average Young's modulus rising from 131 to 157 GPa with increasing Cr^{3+} concentration. The Young's moduli (E) shown in Figure 3(f) obtained by both the ultrasonic reflection method and nanoindentation technique were similar, indicating a high degree of reliability in the results. Additionally, hardness is a key indicator of the ability of TBC materials to resist permanent local deformation[39]. Figures 4(a-e) show the hardness of $(Gd_{1-x}Cr_x)TaO_4$ as measured by nanoindentation. The average Young's modulus increased from 6.8 to 8.3 GPa with rising Cr^{3+} content, as shown in Figure 4(f), but decreased slightly to 7.9 GPa upon reaching the 20% Cr^{3+} content. The primary reason for this hardness enhancement is that the ionic radius of Cr^{3+} is substantially smaller than Gd^{3+}, meaning that the introduction of Cr^{3+} induces lattice distortion, generating an elastic stress field that impedes dislocation slip. Furthermore, the incorporation of Cr^{3+} refined the grain structure, increasing the intergranular boundary area per unit volume. This hinders dislocation motion and enhances the $(Gd_{1-x}Cr_x)TaO_4$ resistance to plastic deformation[40].

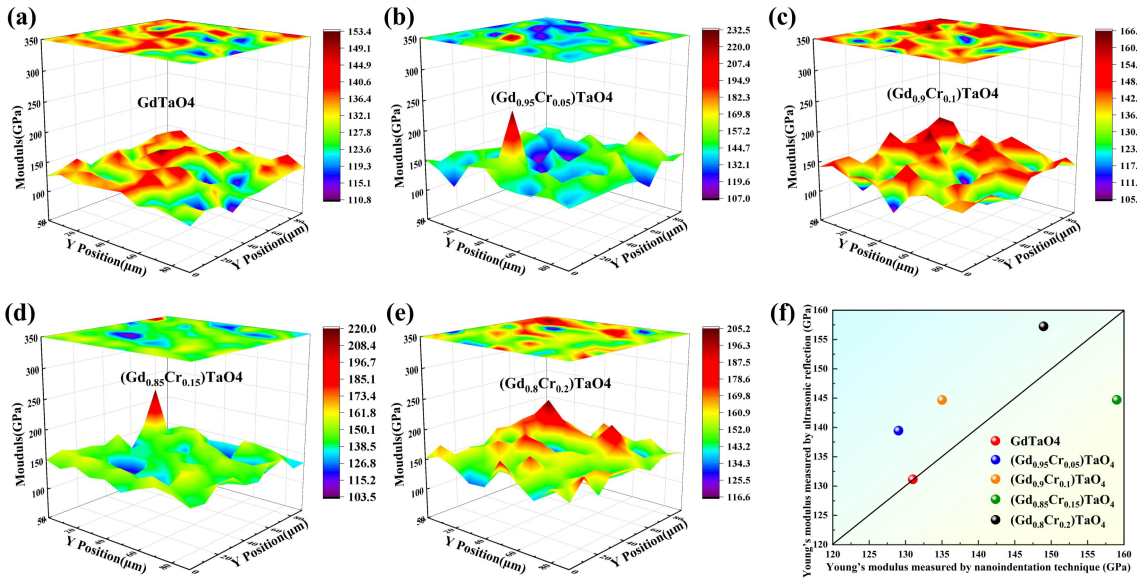

Figure 3. 3D contour map of Young's modulus of $(Gd_{1-x}Cr_x)TaO_4$ ceramics. (a-e) three-dimensional Young's modulus distribution; (f) comparison of average Young's moduli from nanoindentation technique and ultrasonic reflection method.

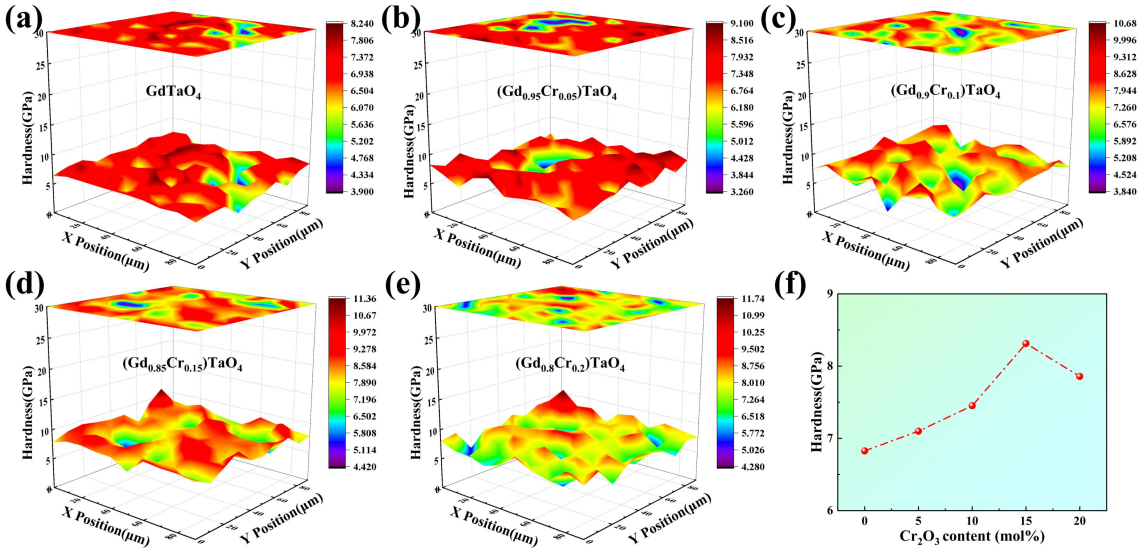

Figure 4. 3D contour map of hardness of $(Gd_{1-x}Cr_x)TaO_4$ ceramics. (a-e) three-dimensional hardness distribution; (f) average hardness diagram.

Thermal properties

Figures 5(a) and (b) show the temperature-dependent thermal diffusivity (α) and thermal conductivity (κ) curves of $(Gd_{1-x}Cr_x)TaO_4$, respectively. The values of α and κ gradually decreased as the temperature increased from room temperature to 1,000 °C [41]. However,

the thermal diffusivity showed a slow upward trend when the temperature exceeded 1,000 °C, indicating that the influence of thermal radiation becomes significant and photon-mediated heat conduction begins to dominate at high temperatures[42]. Additionally, $(Gd_{0.95}Cr_{0.05})TaO_4$ exhibited the lowest thermal conductivity with a value of 1.45 $W \cdot m^{-1} \cdot K^{-1}$ at 1,100 °C among the samples, which was significantly lower than that of 8YSZ with 2.75 $W \cdot m^{-1} \cdot K^{-1}$[43].

The thermal expansion coefficient (TEC) is also one of the primary indicators for thermal barrier coating materials in high-temperature applications. The TEC of ceramic coatings matching with the substrate can contribute to reducing thermal stress and decreasing the risk of coating cracking and peeling during thermal cycling[44]. Figure 5(c) shows that the TEC (9.5-10.5×10^{-6} K^{-1}) of $(Gd_{1-x}Cr_x)TaO_4$ at 1,200 °C was close to that of most alloys (≥ 12×10^{-6} K^{-1})[45,46]. Furthermore, Figure 5(d) shows a steady slope for the thermal expansion rate (dL/dL_0) of $(Gd_{1-x}Cr_x)TaO_4$, meaning that the samples underwent no phase transition or exhibited negligible volume variation due to a phase transition within the temperature range of 200 to 1,200 °C.

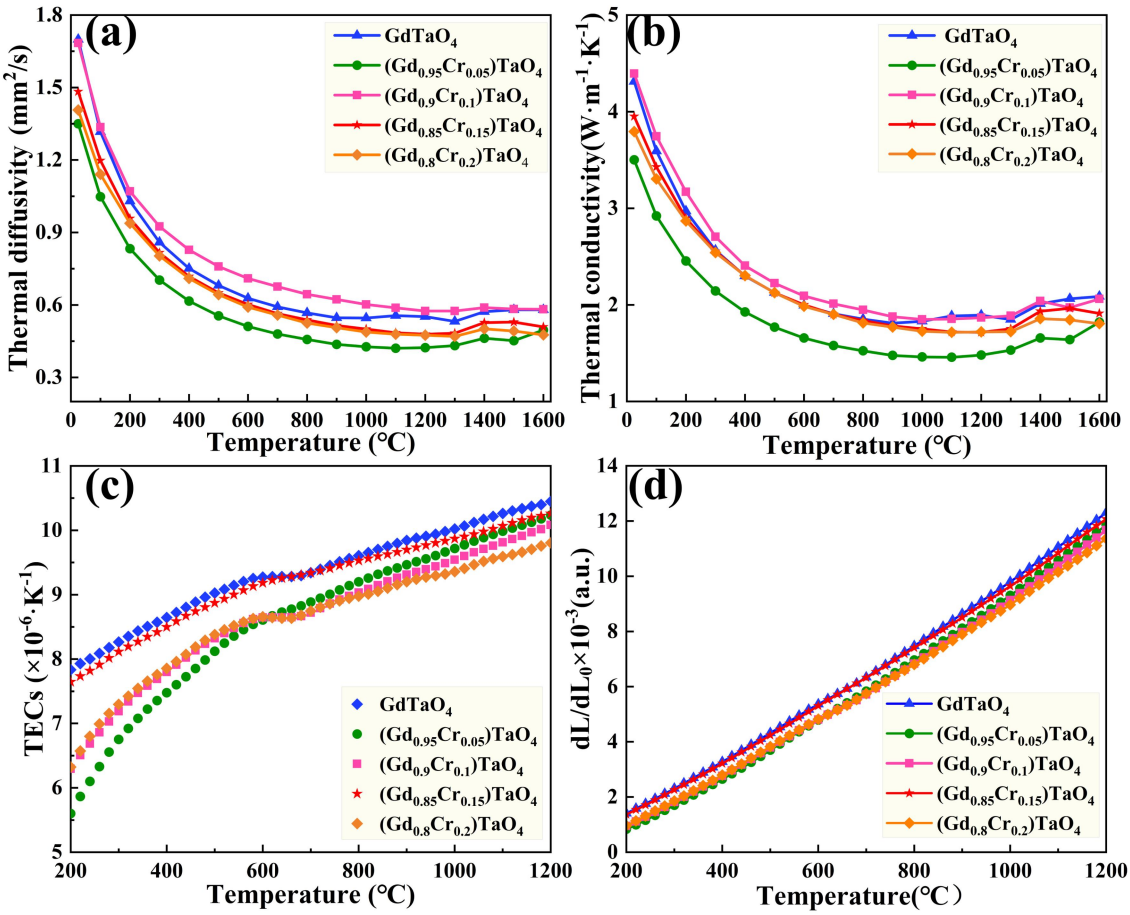

Figure 5. Thermophysical properties. (a) experimental thermal diffusion coefficient; (b) thermal conductivity of corrected porosity; (c) thermal expansion coefficient; (d) thermal expansion rate.

Infrared emissivity

Emissivity is a key parameter for evaluating the IR performance of materials. Figure 6 shows the spectral and average emissivity of $(Gd_{1-x}Cr_x)TaO_4$ for wavelengths of 1-3 and 3-14 μm at 800 °C. Figure 6(a) shows that the high-temperature infrared emissivity spectrum of $(Gd_{1-x}Cr_x)TaO_4$ exhibited periodic oscillations in the 1-1.5 μm range, probably attributable to Fabry-Perot interference of the thermal radiation between parallel interfaces within the material[47]. Figure 6(b) shows that $(Gd_{1-x}Cr_x)TaO_4$ had a sharp absorption peak at a wavelength of 4.2 μm, which was caused by an infrared absorption effect resulting from the presence of H_2O and CO_2 in the atmosphere[36]. The average emissivity results shown in Figure 6(c) and (d) indicated that Cr^{3+} doping significantly enhanced the infrared emissivity of $GdTaO_4$. In particular,

$(Gd_{0.95}Cr_{0.05})TaO_4$ exhibited a relatively high average emissivity, specifically 0.78 in the 1-3 μm band and 0.81 in the 3-14 μm band. Although the infrared emissivity exhibited a slight decrease when the Cr^{3+} content exceeded 10%, the infrared emissivity of $(Gd_{1-x}Cr_x)TaO_4$ at 800 °C still surpassed 0.71, which was significantly higher than that of most reported ceramic materials[48]. These results therefore demonstrated that $(Gd_{1-x}Cr_x)TaO_4$ is an ideal high-temperature thermal protection material.

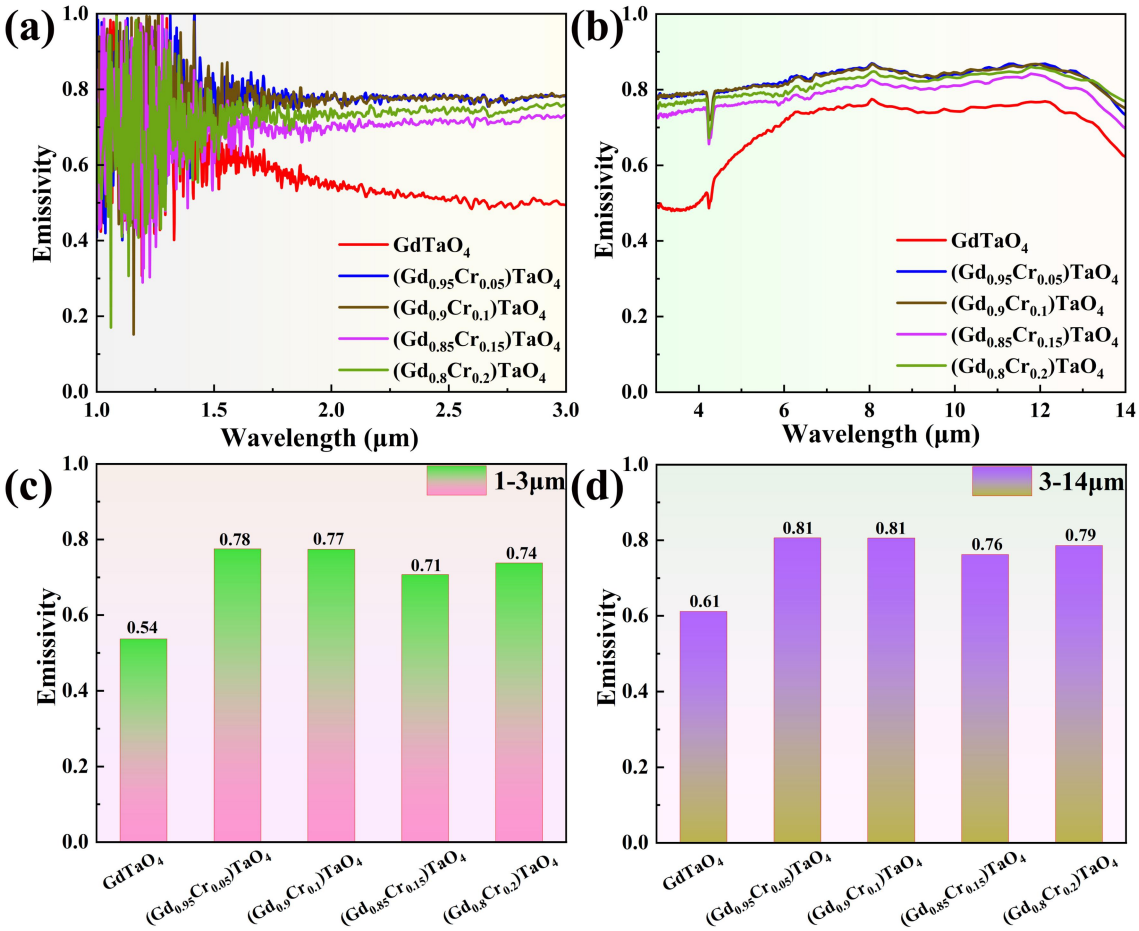

Figure 6. Infrared emissivity of $(Gd_{1-x}Cr_x)TaO_4$ at high temperatures. (a) spectral emissivity at 1-3 μm wavelength range at 800 ℃; (b) spectral emissivity at 3-14 μm wavelength range at 800 ℃; (c) average emissivity in wavelength range of 1-3 μm at 800 ℃; (d) average emissivity in wavelength range of 3-14 μm at 800 ℃.

DISCUSSION

Hierarchical architectures defect

The nanoscale microstructure of $(Gd_{0.95}Cr_{0.05})TaO_4$ was characterized by HAADF-STEM images, as shown in Figure 7(a), where the positions of Gd, Ta, and O atoms are labeled. Closer inspection of the magnified region in Figure 7(b) revealed that the distance separating adjacent tantalum atoms ($d_{Ta\text{-}Ta}$ = 0.097 nm) is less than the separation between rare-earth atom pairs ($d_{Gd\text{-}Gd}$ = 0.117 nm). Furthermore, the atomic-resolution energy dispersive X-ray (EDX) mapping shown in Figure 7(c-f) revealed that Ta and Gd atoms occupied ideal lattice positions, while Cr simultaneously occupied two sublattice sites (rare earth and tantalum sites). The results indicated that Cr atoms have substituted both Ta and Gd atomic positions, resulting in oxygen vacancy defects. The defect chemistry equations in $(Gd_{0.95}Cr_{0.05})TaO_4$ can be represented using Kröger-Vink notation:

$$Cr_2O_3 \xrightarrow{GdTaO_4} Cr_{Gd}^{\times} + Cr_{Ta}^{''} + 3O_O^{\times} + V_O^{\cdot\cdot} \qquad (13)$$

where $Cr_{Gd}^{\times}$ refers to the Cr^{3+} cations occupying the Gd sites in $GdTaO_4$, $Cr_{Ta}^{''}$ denotes the Cr^{3+} cations occupying the Ta sites, $O_O^{\times}$ represents the oxygen atoms occupying oxygen sites and $V_O^{\cdot\cdot}$ indicates oxygen vacancies.

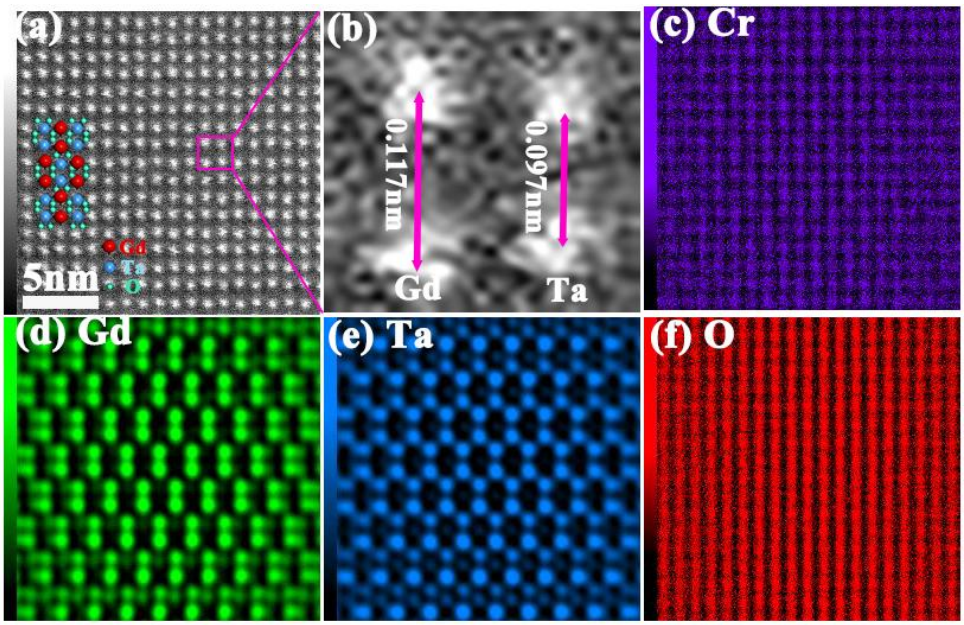

Figure 7. Atomic-resolution HAADF-STEM imaging coupled with EDX elemental

mapping of $(Gd_{0.95}Cr_{0.05})TaO_4$. (a) Atomic-scale HAADF-STEM micrograph acquired along the [001] zone axis; (b) magnified view corresponding to the region in (a); (c) Cr; (d) Gd; (e) Ta; (f) O.

Figure 8 shows the HAADF-STEM pattern of $(Gd_{0.95}Cr_{0.05})TaO_4$ for analyzing dislocation and strain variations. Figure 8(a) shows the arrays embedded in grain boundaries and the enlarged view in Figure 8(b) exhibits the obvious positive-blade dislocations. The occurrence of positive-blade dislocations was primarily attributed to the introduction of Cr^{3+} ions, which caused ion radius mismatch and generated lattice strain near the doping sites[49]. Therefore, the significant macroscopic internal stress was developed within the grains. The strain distribution was calculated by geometric phase analysis (GPA) and the corresponding strain mapping is shown in Figure 8(c) and (d). GPA maps in the *x*- (ε_{xx}) and *y*-axis (ε_{yy}) directions indicate concentrations of high strain close to the dislocation core. Cha *et al.*[50] also reported similar results for Cl-doped SnSe.

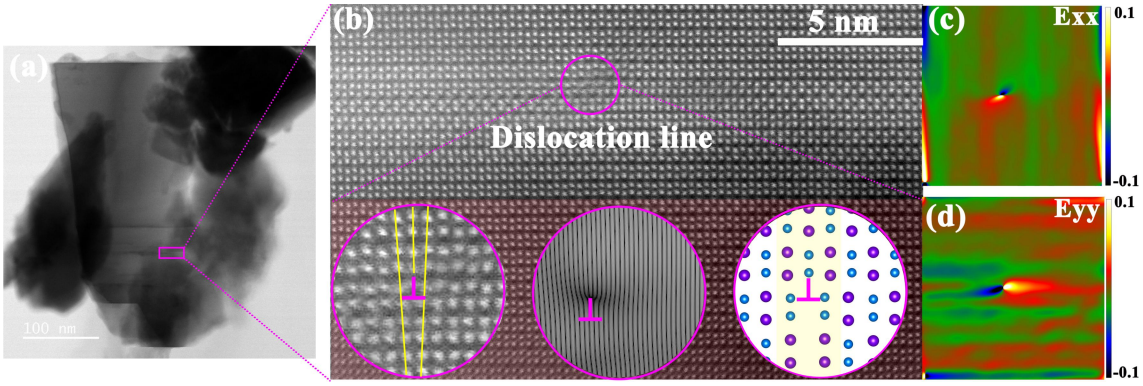

Figure 8. Dislocation analysis of $(Gd_{0.95}Cr_{0.05})TaO_4$. (a) ADF image of dislocation lines at macroscopic level; (b) enlarged image of (a); (c-d) HAADF-STEM images were processed by geometric phase analysis (GPA).

Figures 9(a-e) show the grain morphology of $(Gd_{1-x}Cr_x)TaO_4$. The boundaries between the grains were clearly visible, and there were no obvious pores, indicating that $(Gd_{1-x}Cr_x)TaO_4$ exhibited high density. This result was consistent with the conclusions

obtained from the Archimedes method (porosity ≤ 5%). The lines depicted in Figure 9(a_1-e_1) represent ferroelastic domain structures with stripe-like patterns placed in different directions on different grain surfaces, as also reported by Wang *et al.*[43]. The typical ferroelastic domain structure enabled the absorption of mechanical stress, enhanced fracture toughness and also contributed to increased low-frequency phonon scattering intensity whilst reducing thermal conductivity[13,51,52]. The distribution of grain sizes shown in Figure 9(a_2-e_2) was obtained through Image-Pro Plus 6.0. The grain size of $(Gd_{1-x}Cr_x)TaO_4$ decreased after doping Cr_2O_3, which may be attributed to the grain boundary pinning effects resulting from Cr^{3+} doping[53]. A high concentration of pinning points reduced grain boundary mobility, thereby inhibiting grain growth and leading to grain refinement[54]. The EDS image in Supplementary Figure 1 reveals that the elements in $(Gd_{1-x}Cr_x)TaO_4$ do not exhibit obvious segregation.

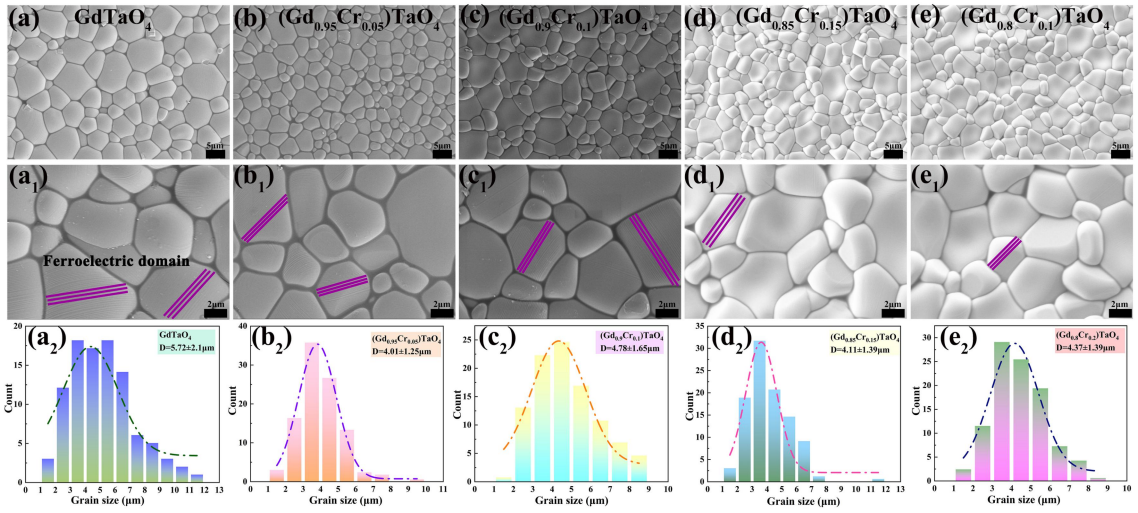

Figure 9. Microscopic structure and grain size statistics of $(Gd_{1-x}Cr_x)TaO_4$. (a-e) characterization of grain morphology; (a_1-e_1) ferroelastic domain structure; (a_2-e_2) grain size distribution and Gaussian distribution diagram.

Origin of low thermal conductivity

The variation of thermal conductivity is primarily governed by the scattering intensities of phonons and photons in ceramic materials. First, the Debye model was used to calculate the phonon thermal conductivity (κ_{Pho}) to evaluate the contribution of phonons

to the thermal conductivity[55]:

$$\kappa_{Pho}=\frac{1}{3}cvl \quad (14)$$

where c is the specific heat capacity per unit volume, v is the average speed of sound and l is the average free path. Supplementary Figure 2(b) shows the phonon thermal diffusivity of $(Gd_{1-x}Cr_x)TaO_4$, which was obtained by fitting the inverse of the experimental thermal diffusivity from room temperature to 1,600 °C. As shown in Figure 10(a), the κ_{Pho} values of $(Gd_{0.95}Cr_{0.05})TaO_4$ at room temperature and 1,600 °C were 2.96 and 1.02 $W\cdot m^{-1}\cdot K^{-1}$, respectively. The introduction of 5 mol% Cr_2O_3 significantly reduced the phonon thermal conductivity of rare-earth tantalate by 24.6% at room temperature and by 16.5% at 1,600 °C compared to $GdTaO_4$. Furthermore, the Clarke model was employed to evaluate the ultimate thermal conductivity of $(Gd_{1-x}Cr_x)TaO_4$ at high temperatures[56]:

$$\kappa_{min}=0.84\kappa_B N_A^{\frac{2}{3}}\frac{m^{\frac{2}{3}}\rho^{\frac{1}{6}}E^{\frac{1}{2}}}{M^{\frac{2}{3}}} \quad (15)$$

where k_B, M, m, n, E, ρ and N_A represent the Boltzmann constant, atomic mass in a single cell, number of atoms in a molecular formula, atomic number density, Young's modulus, density and Avogadro's constant, respectively. Figure 10(b) demonstrates that the phonon thermal conductivity of $(Gd_{1-x}Cr_x)TaO_4$ at 1,600 °C approaches the ultimate value derived from the Clarke model.

Second, the following formulae were used to calculate the radiative thermal conductivity (k_{rad}) to evaluate the contribution of photons to the thermal conductivity coefficient[57-60]:

$$E_r=\frac{4\sigma n^3 T^4}{c} \quad (16)$$

$$C_R=\frac{16\sigma n^3 T^4}{c} \quad (17)$$

$$k_{rad}=\frac{16n^2\sigma T^3}{3\beta_R} \quad (18)$$

$$\beta_R=\alpha+\beta \quad (19)$$

where E_r, C_R, k_{rad}, σ, n, c, β_R, α and β represent the energy radiated per unit volume by a blackbody, the volumetric specific heat capacity corresponding to the energy required to raise the temperature of the radiation, the thermal conductivity of radiation, the Stefan-Boltzmann constant (1.37×10^{-12} cal/cm^2·s·K^4), the refractive index, the speed of light (3×10^{10} cm/s), the extinction coefficient, the scattering coefficient and the absorption coefficient, respectively. The n and β_R of $(Gd_{1-x}Cr_x)TaO_4$ at 1-5 μm are shown in Supplementary Table 2.

As shown in Figures 10(c) and (d), the phonon thermal conductivity dominated the total heat transfer energy at low temperatures. However, the contribution of the photon thermal conductivity increased with rising temperature[19]. The theoretical total thermal conductivity, including the contribution of phonons and photons, exceeded the experimentally thermal conductivity. The deviation primarily originated from the significant coupling and interaction mechanisms between phonons and photons [61, 62]. The process not only failed to enhance heat transfer efficiency but also reduced the overall thermal conductivity due to energy dissipation effects. The phonons emit photons, which are absorbed by the medium excite phonons, forming a bidirectional energy coupling mechanism under high-temperature conditions [63]. Therefore, the theoretical total thermal conductivity cannot be represented by the simple summation of the phonon and photon thermal conductivities.

In addition, the thermal conductivity of $(Gd_{0.95}Cr_{0.05})TaO_4$ was higher than that of

$GdTaO_4$. The reason was that the introduction of Cr^{3+} induced *d-d* electron transitions, which generated the new absorption bands in the infrared region, thus enhancing thermal radiation. Cr^{3+} doping induces the increase of the radiative thermal conductivity, while simultaneously enhancing phonon scattering and phonon-photon coupling effects. This leads to a synergistic mechanism that reduces the thermal conductivity, ultimately achieving the total thermal conductivity reduction.

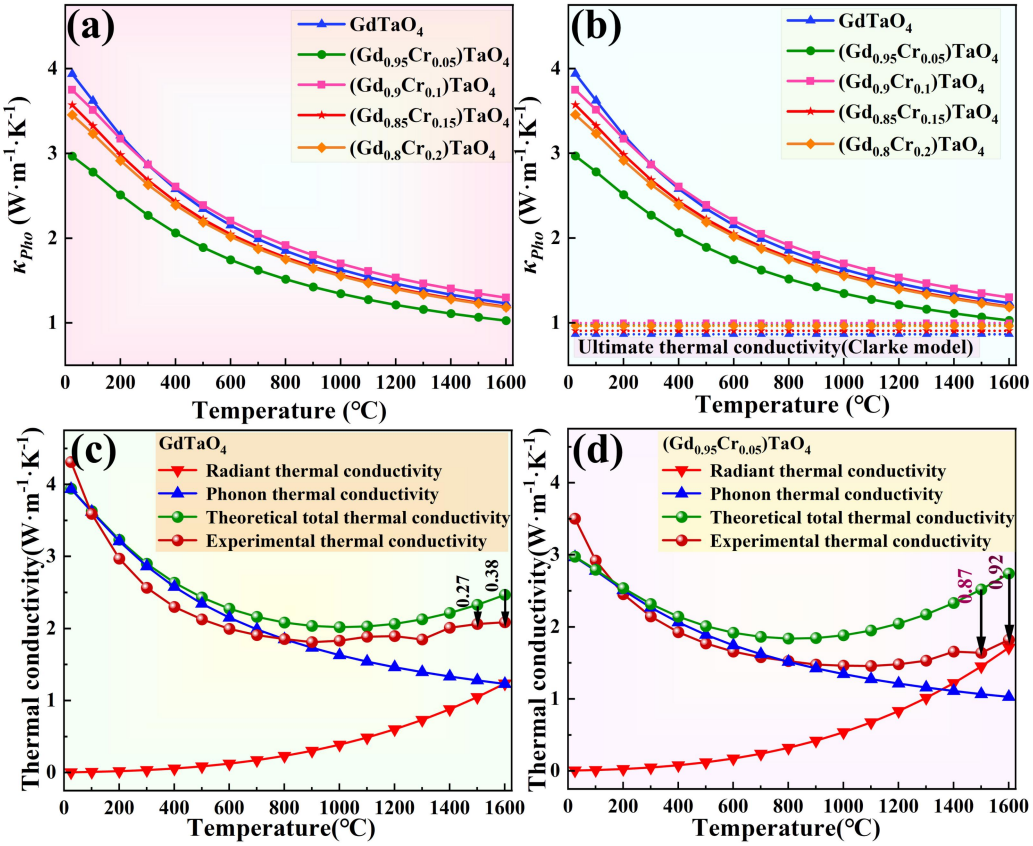

Figure 10. Thermal transport mechanism. (a) phonon thermal conductivity of $(Gd_{1-x}Cr_x)TaO_4$; (b) Clarke model of $(Gd_{1-x}Cr_x)TaO_4$; (c) and (d) corresponding to the thermal conductivity of $GdTaO_4$ and $(Gd_{0.95}Cr_{0.05})TaO_4$, including phonon-, radiative-, experimental-, and theoretical total thermal conductivity.

Additionally, multiple lattice defects interact synergistically in Cr-doped $GdTaO_4$ ceramics, significantly enhancing multi-frequency phonon scattering, thereby leading to a significant reduction in lattice thermal conductivity (κ_l). To analyze the mechanism of low thermal conductivity of Cr^{3+}-doped $GdTaO_4$, the contributions of various defects to

phonon scattering were analyzed through Debye-Callaway model[43]:

$$\kappa_l = \frac{k_B}{2\pi^2 v_m}\left(\frac{k_B T}{h}\right)^3 \int_0^{\theta_D/T} \tau_{tot}(x)\frac{x^4 e^x}{(e^x-1)^2}\,dx \quad (20)$$

where $x = \omega/k_B T$ and h and ω correspond to Planck's constant and phonon angular frequency, respectively. Furthermore, the total phonon relaxation time (τ_{tot}^{-1}) was expressed as the inverse sum of the relaxation times of various scattering mechanisms[43]:

$$\tau_{tot}^{-1} = \tau_U^{-1} + \tau_{PD}^{-1} + \tau_D^{-1} + \tau_{GB}^{-1} + \tau_{DB}^{-1} \quad (21)$$

where τ_U^{-1}, τ_{PD}^{-1}, τ_D^{-1}, τ_{GB}^{-1} and τ_{DB}^{-1} represent the contributions of Umklapp processes, point defects, dislocation scattering, grain boundaries and domain boundaries to the relaxation time, respectively.

The inverse relaxation time τ_U^{-1}, which accounts for phonon-phonon scattering in Umklapp processes, is determined using the equation below[64]:

$$\tau_U^{-1} = \frac{2}{(6\pi^2)^{\frac{1}{3}}}\frac{k_B \overline{V}^{\frac{1}{3}}\gamma^2\omega^3 T}{\overline{M}v_m^3} \quad (22)$$

where V represents the average atomic volume, M denotes the average atomic mass, and the Grüneisen parameter is expressed by γ. For point defect processes, the addition of Cr^{3+} results in point defects in Cr-doped $GdTaO_4$, with the following relaxation times[65]:

$$\tau_{PD}^{-1} = \frac{\overline{V}\omega^4}{4\pi v^3} f_i\left[\varepsilon\left(\frac{r_{i,s}-\overline{r_s}}{\overline{r_s}}\right)^2 + \left(\frac{M_{i,s}-\overline{M_s}}{\overline{M_s}}\right)^2\right] \quad (23)$$

where f_i represents the defect content within the lattice; $r_{i,s}$ and r_s correspond to the ionic radius of the ith constituent and the mean ionic radius at crystallographic position s,

respectively; and $M_{i,s}$ and $\overline{M_s}$ refer to the mass of the ith species and the average mass at position s. The dislocation (D) processes, as one-dimensional defects, correspond to the relaxation time formula as follows[66]:

$$\tau_D^{-1}=N_D\frac{\frac{4}{\sqrt{3}}\omega^3}{v^2}+0.6\times B_D^2 N_D\gamma^2\omega\left[\frac{1}{2}+\frac{1}{24}\left(\frac{1-2\xi}{1-\xi}\right)^2\left(1+\sqrt{2}\left(\frac{v_l}{v_t}\right)^2\right)^2\right] \quad (24)$$

where N_D is the dislocation density, r denotes the core radius of dislocations, B_D represents the Burgers vector magnitude, and ξ corresponds to Poisson's ratio. The scattering events at grain boundaries (GB) and domain boundaries (DB), as two-dimensional defects, correspond to the relaxation time formulae as follows[67]:

$$\tau_{GB}^{-1}=\frac{v_m}{d_{GB}} \quad (25)$$

$$\tau_{DB}^{-1}=A\frac{v_m}{d_{DB}} \quad (26)$$

where d_{GB} and d_{DB} denote the grain size and the width of domain boundaries, respectively, and A represents a fitting parameter associated with domain boundaries, taken as 0.1[43]. Figure 11(a) illustrates that Umklapp and point defect scattering are the dominant scattering mechanisms for high-frequency phonons, with their relaxation times satisfying the frequency-dependent relationships $\tau_U^{-1}\propto\omega^3$ and $\tau_{PD}^{-1}\propto\omega^4$, respectively. Dislocation scattering (D) primarily targets low to mid- and high-frequency phonons, following the frequency-dependent relationships $\tau_D^{-1}\propto\omega^3$and $\tau_D^{-1}\propto\omega^1$, respectively. Grain boundary scattering (GB) and domain boundary scattering (DB), as a typical interface scattering mechanism, primarily target low-frequency phonons, satisfying the relationship $\tau_{GB}^{-1}\propto\omega^0$. Furthermore, employing the Debye model, the κ_l of $(Gd_{0.95}Cr_{0.05})TaO_4$ was computed under various conditions as presented in Figure 11(b), aiming to assess how multiscale lattice defects contribute to the reduction in κ_l. The parameters adopted for phonon transport modeling are

summarized in Supplementary Table 2. As shown in Figure 11(c), the fitted lattice thermal conductivity curves closely aligned with the phonon thermal conductivity, indicating the significant contribution of multi-dimensional lattice defects in enhancing phonon scattering and reducing thermal conductivity.

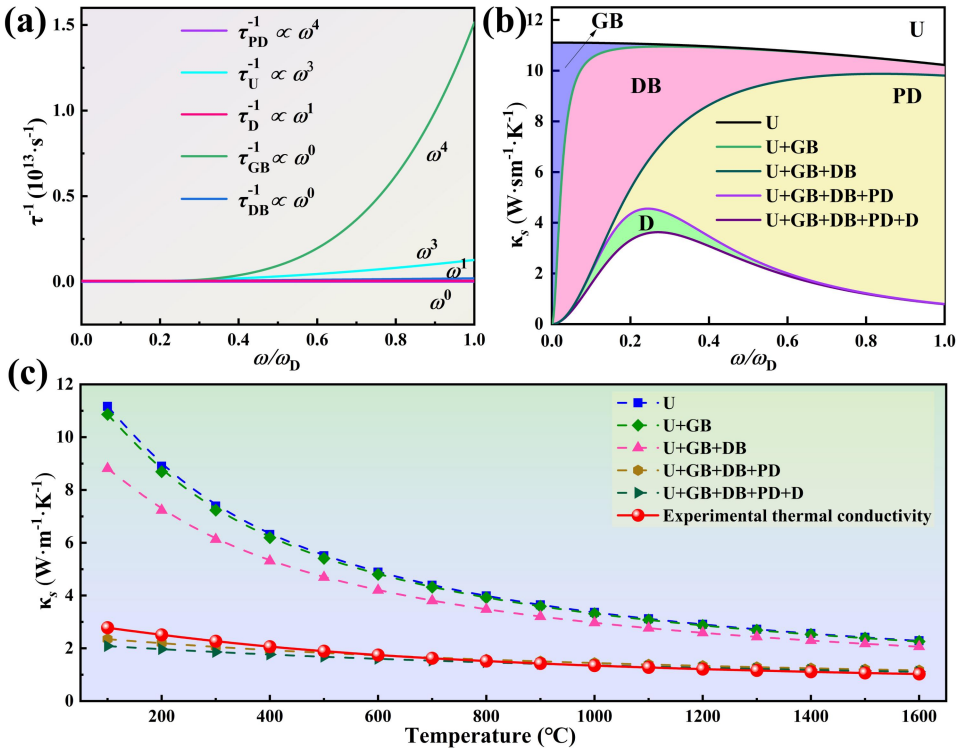

Figure 11. Thermal transport properties with different phonon scattering mechanisms for $(Gd_{0.95}Cr_{0.05})TaO_4$. (a) characteristic relaxation times of phonons as a function of angular frequency measured at 298 K; (b) frequency-dependent lattice thermal conductivity at 298 K, considering contributions from various scattering mechanisms, namely Umklapp (*U*), grain boundary (*GB*), domain boundary (*DB*), point defect (*PD*), and dislocation (*D*) processes; (c) temperature-dependent lattice thermal conductivity derived from fitting with the Debye model.

Origin of high emissivity

In the near-infrared wavelength range, the infrared radiation behavior of materials is dominated by free carrier and vibrational absorption[68]. First, free carrier absorption depends on the oxygen vacancy concentration and the band gap value. On the one hand, the concentration of oxygen vacancies, which act as charge carriers, plays a determining

role in the radiative performance of materials within the near- to mid-infrared region. Specifically, a higher vacancy content leads to more pronounced radiation enhancement[69-71]. The results of Figure 8 infer the existence of oxygen vacancies, indicating that oxygen vacancies in $(Gd_{1-x}Cr_x)TaO_4$ caused free carrier absorption. On the other hand, a narrower band gap corresponds to a reduced energy separation between the valence and conduction bands[72], thereby lowering the barrier for electronic excitation, which enhances accessibility for intraband transitions and subsequently promotes free carrier absorption.

The band structure of $(Gd_{1-x}Cr_x)TaO_4$ is shown in Figure 12, where the Fermi level is aligned to 0 eV, and the conduction band resides above the Fermi level, while the valence band lies below it; the band gap corresponds to the energy difference between the top of the valence band and the bottom of the conduction band. Figure 12(a) show the intrinsic band gap of $GdTaO_4$ was ~4.10 eV, slightly less than the 4.86 eV reported in the literature[73,74]. Figures 12(b-e) show that the band gap value of the doped material was reduced, with the doping of transition metal Cr^{3+} ions introducing impurity levels within the band gap and effectively reducing the optical band gap. Figure 12(f) shows that the band gap experienced a significant reduction from 4.1 to 0.9 eV with increasing Cr content. Furthermore, the emissivity within the 1-14 μm range increased from 0.59 to 0.80 as the band gap decreased for $(Gd_{1-x}Cr_x)TaO_4$. These results demonstrated the close correlation between enhanced emissivity and narrowed band gap. It was noteworthy that the emissivity showed a slight decrease when the Cr^{3+} doping concentration exceeded 10%, which was the result of the concentration quenching effect induced by high doping concentrations[68,75]. Another reason for this was that the excessive Cr^{3+} ions that may promote point defect agglomeration, the formation of $(Gd_{1-x}Cr_x)TaO_4$ non-radiative recombination centers, and the reduction in the efficiency of photon absorption and re-radiation[76,77].

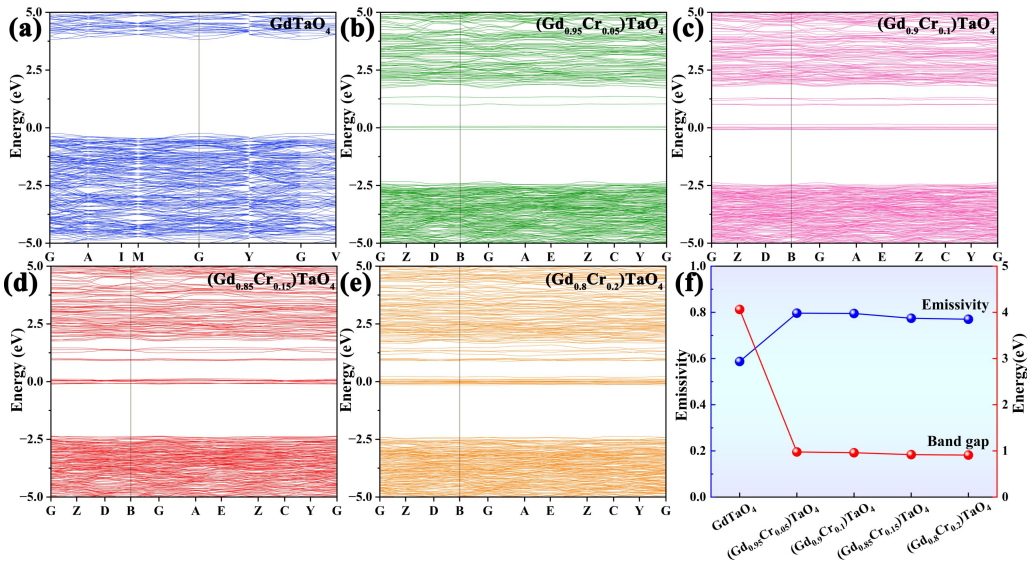

Figure 12. Band structure of $(Gd_{1-x}Cr_x)TaO_4$. (a) $GdTaO_4$; (b) $(Gd_{0.95}Cr_{0.05})TaO_4$; (c) $(Gd_{0.9}Cr_{0.1})TaO_4$; (d) $(Gd_{0.85}Cr_{0.15})TaO_4$; (e) $(Gd_{0.8}Cr_{0.2})TaO_4$; (f) band gap width and the average emissivity within the 1-14 μm wavelength range at 800 °C.

Second, Cr doping induces variations in bond lengths and angles within $GdTaO_4$, thereby enhancing the lattice distortion and vibration absorption. Evidently, $(Gd_{0.95}Cr_{0.05})TaO_4$ exhibited the greatest lattice distortion [Table 3] and corresponded to the highest emission intensity [Figure 12(f)]. According to the theory of lattice vibrations, adjustments to dipole moments brought by atomic or molecule oscillations inside materials produce infrared radiation. The reduction in vibrational symmetry within the crystal structure enhanced the dipole moment variations, subsequently amplifying the intensity of infrared radiation[78].

The results of the above analysis indicated that the free carrier absorption caused by band gap size and vibrational absorption induced by lattice distortion co-enhanced the emissivity of $(Gd_{1-x}Cr_x)TaO_4$. As shown in Figure 13(a), the infrared absorption process involved electrons being excited by photons within the infrared radiation, absorbing energy to transition to higher-energy conduction band levels. However, the state was extremely unstable, and the electron rapidly transitioned back from the conduction band to the valence band, releasing the excess energy into the environment in the form of

radiant heat. Figure 13(b) shows the introduction of Cr^{3+} ions to displace Gd^{3+} sites within $GdTaO_4$ produced significant local lattice distortion. The disparity in ionic radius and charge distribution between Cr^{3+} and Gd^{3+} ions induced the distortion. The distortion disrupted the periodicity and symmetry of the original lattice, increasing the anharmonicity of lattice vibrations, hence promoting the excitation and coupling of vibrational modes within the infrared band[68].

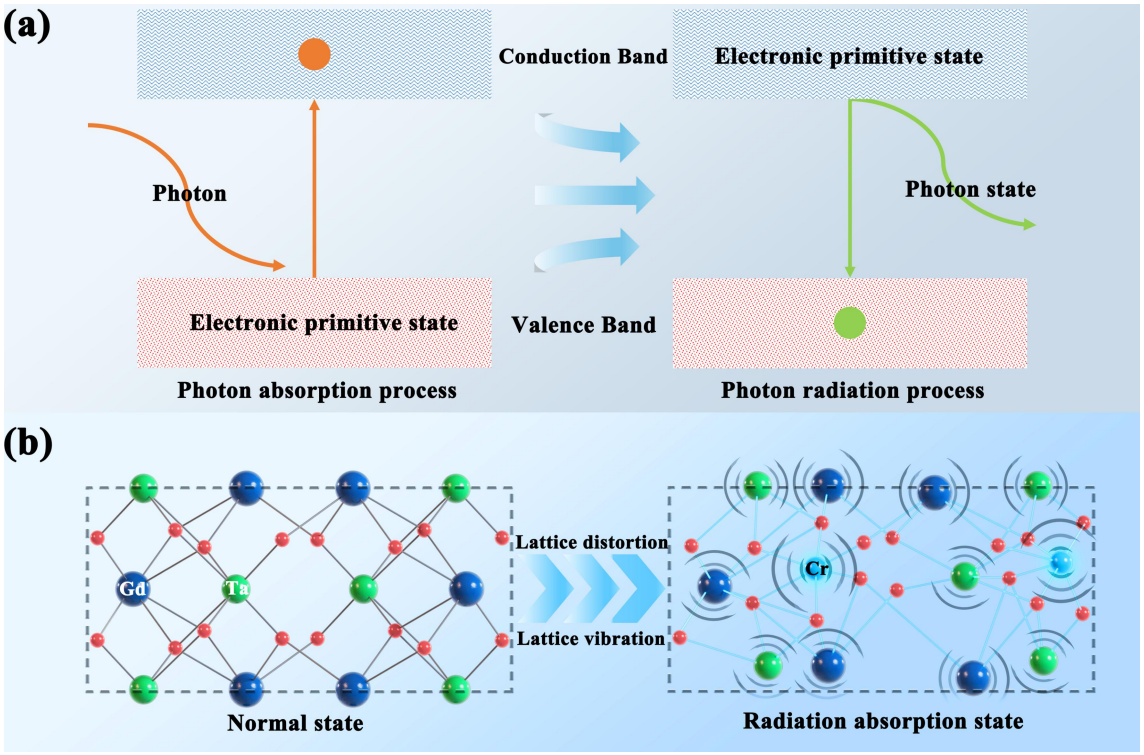

Figure 13. High emissivity mechanism. (a) schematic diagram of photon radiation; (b) lattice vibration mechanism.

CONCLUSION

Novel rare-earth tantalate ceramic $(Gd_{1-x}Cr_x)TaO_4$ synthesized via the solid-state method exhibited excellent thermal protection properties. The main conclusions were as follows:

(1) The results of thermal insulation testing showed that $(Gd_{0.95}Cr_{0.05})TaO_4$ had higher temperature drop gradients than that of conventional 8YSZ and $La_2Zr_2O_7$ materials, benefiting from the low intrinsic thermal conductivity with 1.03 $W \cdot m^{-1} \cdot K^{-1}$ at 1,600 °C

and high emissivity with 0.81 across the 1-14 μm wavelength range at 800 °C.

(2) Cr atoms occupied Ta and RE sites in the $GdTaO_4$ lattice to generate oxygen vacancies, whereas the disparity in atomic radii among Cr, Ta and RE atoms produced dislocations, and stress concentrations formed near the dislocation cores.

(3) The ultralow thermal conductivity of $(Gd_{0.95}Cr_{0.05})TaO_4$ originated from the synergistic scattering of phonons by multiscale defects, including the point defects that target high-frequency phonon scattering, the dislocations and domain boundaries that target medium- and low-frequency phonon scattering, and the grain boundaries that target low-frequency phonon scattering. Moreover, the enhanced phonon-photon coupling effect at elevated temperatures further suppressed thermal transport rates.

(4) The high emissivity of $(Gd_{0.95}Cr_{0.05})TaO_4$ from the high free carrier absorption depended on the high oxygen vacancy concentration and a narrow band gap of 0.9 eV, as well as high vibrational absorption resulting from the severe lattice distortion (1.533%).

(5) The Young's modulus and hardness of $(Gd_{0.95}Cr_{0.05})TaO_4$ were 129 and 7.1 GPa, respectively.

DECLARATIONS

Authors' contributions

Conceived and designed the study: MY.Z, MZ.P, J.W, J.F;

Provided supervision and project administration: J.W, J.F;

Wrote and revised the manuscript: MY.Z, BB.W, J.W, Z.G, J.F;

Collected, organized, and analyzed the validation datasets: JW.Y, RH.L, HY.L, FC.Q, P.W;

All authors read and approved the final manuscript.

Availability of data and materials

The data that support the findings of this study are available from the corresponding author upon reasonable request.

Financial support and sponsorship

This research was supported by the National Natural Science Foundation of China (52402077), Yunnan Fundamental Research Projects (202501AU070113, 202501AT070624, 202401BE070001-043), Open Fund of Zhijian Laboratory (Rocket Force University of Engineering), No.2025-ZJSYS-KF-03, Scientific Research Fund Project of the Department of Education of Yunnan Province (2025J0106).

Conflicts of interest

All authors declared that there are no conflicts of interest.

Conflicts of interest

All authors declared that there are no conflicts of interest.

Ethical approval and consent to participate

Not applicable.

Consent for publication

Not applicable.

Copyright

© The Author(s) 2026.

REFERENCES

1. Kumar, S, Mahulikar, S P. Reconstruction of aero-thermal heating and thermal protection material response of a Reusable Launch Vehicle using inverse method. *Appl. Therm. Eng.* **2016**, *103*, 344-55. [DOI: 10.1016/j.applthermaleng.2016.04.100]

2. Wang, S.; Ye, Z.; Ge, Y.; et al., High temperature oxidation behavior at 1250 °C: A new multilayer modified silicide coating design strategy on niobium alloys. *J. Mater. Sci. Technol.* **2025**, *210*, 159-69. [DOI: 10.1016/j.jmst.2024.04.084]

3. Zhao, Q.; Wang, S.; Chen, G.; et al., La_2Hf2O7 Based TBC Materials with Near-Infrared Ultra-Low Transmittance for Thermal Radiation Shielding. *Adv. Opt. Maters.* **2025**, *13*, 2401768. [DOI: 10.1002/adom.202401768]

4. Yang, L-Y.; Dong, S.; Cui, T-Y.; et al., Novel gradient ZrB2-MoSi2-SiC dense layer with enhanced emissivity and long-term oxidation resistance at ultra-high temperatures. Rare. Metals. 2025, 44, 2043-58. [DOI: 10.1007/s12598-024-02959-4]

5. Tang, K.; Wang, X.; Dong, K.; et al., A thermal radiation modulation platform by emissivity engineering with graded metal-insulator transition. Adv. Mater. 2020, 32, 1907071.[PMID: 32700403 DOI: 10.1002/adma.201907071]

6. Ding, S.; Mao, J.; Zeng, X, Cheng, X. Enhanced infrared emission property of NiCr spinel coating doped with MnO2 and rare-earth oxides. Surf. Coat. Tech. 2018, 344, 418-22.[DOI: 10.1016/j.surfcoat.2018.03.059]

7. Liu, Y.; Chu, K.; Zhou, Y.; et al., Discovery of orthorhombic perovskite oxides with low thermal conductivity by first-principles calculations. J. Adv. Ceram. 2022, 11, 1596-603.[DOI: 10.1007/s40145-022-0632-0]

8. Yin, Q.; Shen, K-H.; Wang, Y, Xing, Y-Z. Research progress of rare earth zirconate thermal barrier coating ceramic materials. *Mater. Today. Commun.* **2025**, *42*, 111579. [DOI: 10.1016/j.mtcomm.2025.111579]

9. Wang, X.; Xue, Z.; Zhou, Z.; Byon, E, Zhang, S. Influence of $Yb_2Si_2O_7$ doping concentration on mechanical properties and thermal conductivity of Yb_2SiO_5-$Yb_2Si_2O_7$ composite ceramics. *J. Alloy. Compd.* 2021, *889*, 161718.

10. Tian, Z.; Zheng, L.; Wang, J.; et al., Theoretical and experimental determination of the major thermo-mechanical properties of RE_2SiO_5 (RE= Tb, Dy, Ho, Er, Tm, Yb, Lu, and Y) for environmental and thermal barrier coating applications. *J. Eur. Ceram. Soc.* **2016**, *36*, 189-202. [DOI: 10.1016/j.jeurceramsoc.2015.09.013]

11. Zhao, Z.; Xiang, H.; Chen, H.; et al., High-entropy $(Nd_{0.2}Sm_{0.2}Eu_{0.2}Y_{0.2}Yb_{0.2})_4Al_2O_9$ with good high temperature stability, low thermal conductivity, and anisotropic thermal

expansivity. *J. Adv. Ceram.* **2020**, *9*, 595-605. [DOI: 10.1007/s40145-020-0399-0]

12. Huang, J.; Zhang, X.; Fang, T.; et al., Effect of La content on infrared radiation performance of lanthanum-cerium oxides for high temperature application. *Opt. Mater.* **2020**, *108*, 110211. [DOI: 10.1016/j.optmat.2020.110211]

13. Zhang, P.; Feng, Y.; Li, Y.; et al., Thermal and mechanical properties of ferroelastic $RENbO_4$ (RE= Nd, Sm, Gd, Dy, Er, Yb) for thermal barrier coatings. *Scripta. Mater.* **2020**, *180*, 51-6. [DOI: 10.1016/j.scriptamat.2020.01.026]

14. Qu, C.; Chen, L.; Lv, L.; et al., Low thermal conductivity and anisotropic thermal expansion of ferroelastic $(Gd_{1-x}Y_x)TaO_4$ ceramics. *J. Adv. Ceram.* **2022**, *11*, 1696-713. [DOI: 10.1007/s40145-022-0641-z]

15. Virkar, A V, Matsumoto, R L. Ferroelastic domain switching as a toughening mechanism in tetragonal zirconia. *J. Am. Ceram. Soc.* **1986**, *69*, C-224-6. [DOI: 10.1111/j.1151-2916.1986.tb07341.x]

16. Li, J.; Zhou, Q.; Yang, L.; et al., Ferroelastic deformation mechanism and mechanical properties of [001]-oriented YSZ film by indentation. *J. Alloy. Compd.* **2021**, *889*, 161557. [DOI: 10.1016/j.jallcom.2021.161557]

17. Tian, J.; Chen, L.; Chen, X.; et al., Regulation of crystal and microstructures of $RETaO_4$ (RE = Nd, Sm, Gd, Ho, Er) powders synthesized via co-precipitation. *J. Rare. Earth.* **2025**, *43*, 1246-55. [DOI: 10.1016/j.jre.2024.06.032]

18. Wang, X.; Long, Z.; Qian, W.; et al., Influence of $GdTaO_4$ doping concentration on thermophysical and mechanical properties of $GdPO_4/GdTaO_4$ composites. *Ceram. Int.* **2023**, *49*, 18334-42. [DOI: 10.1016/j.ceramint.2023.02.205]

19. Wang, J.; Li, J.; Jiang, C.; et al., Feng, J. Advanced rare earth tantalate $RETaO_4$ (RE=Dy, Gd and Sm) with excellent oxygen/thermal barrier performance. *J. Rare. Earth.* **2024**, *42*, 1595-603. [DOI: 10.1016/j.jre.2024.05.012]

20. Meng, M.; Liu, L.; Liu, Y, Ma, Z. The effect of Mg^{2+} doping on the infrared emissivity of $LaCrO_3$ perovskites. *Ceram. Int.* **2023**, *49*, 14997-5002. [DOI: 10.1016/j.ceramint.2023.01.082]

21. Sun, P.; Hu, P.; Liu, Y.; et al., Broadband emissions from $Lu_2Mg_2Al_2Si_2O_{12}$: Ce^{3+} plate ceramic phosphors enable a high color-rendering index for laser-driven lighting. *J.*

Mater. Chem. C. **2020**, *8*, 1405-12. [DOI: 10.1039/C9TC06068E]

22. Yuan, X.; Wang, Q.; Wu, R.; et al., Environment-friendly Ca^{2+}/Cr^{3+} co-doping $LaAlO_3$ ceramics with excellent infrared radiation performance for energy-saving. *J. Adv. Ceram.* **2025**, *14*. [DOI: 10.26599/JAC.2024.9221017]

23. Deng, Y.; Zhang, K.; Shi, X.; et al., Exploring the underlying mechanisms behind the increased far infrared radiation properties of perovskite-type Ce/Mn co-doped ceramics. *Mater. Res. Bull.* **2019**, *109*, 233-9. [DOI: 10.1016/j.materresbull.2018.09.042]

24. Huang, J.; Fan, C.; Song, G.; et al., Enhanced infrared emissivity of CeO_2 coatings by La doping. *Appl. Surf. Sci.* **2013**, *280*, 605-9. [DOI: 10.1016/j.apsusc.2013.05.034]

25. Ma, Y-H.; Liu, Z-G.; Ouyang, J-H, Jin, Y-J. Influence of TiO_2 doping on thermo-optical properties of pyrochlore $Sm_2(Zr_{1-x}Ti_x)_2O_7$ ($0 \leq x \leq 0.15$) ceramics. *Ceram. Int.* **2016**, *42*, 14749-53. [DOI: 10.1016/j.ceramint.2016.06.102]

26. Luo, X.; Huang, R.; Xu, C.; et al., Designing high-entropy rare-earth zirconates with tunable thermophysical properties for thermal barrier coatings. *J. Alloy. Compd.* **2022**, *926*, 166714. [DOI: 10.1016/j.jallcom.2022.166714]

27. Wang, J.; Jin, Q.; Song, J.; et al., Multiscale defect-mediated thermophysical properties of high-entropy ferroelastic rare-earth tantalates. *Ceram. Int.* **2023**, *49*, 40019-30. [DOI: 10.1016/j.ceramint.2023.09.331]

28. Wang, J.; Chong, X.; Lv, L.; et al., High-entropy ferroelastic $(10RE_{0.1})TaO_4$ ceramics with oxygen vacancies and improved thermophysical properties. *J. Mater. Sci. Technol.* **2023**, *157*, 98-106. [DOI: 10.1016/j.jmst.2022.12.027]

29. Wang, S.; Wang, Y.; Chen, G.; et al., High-temperature broadband infrared radiation from rare earth monosilicate-based ceramics. *J. Eur. Ceram. Soc.* **2024**, *44*, 6510-7. [DOI: 10.1016/j.jeurceramsoc.2024.03.061]

30. Wang, S.; Ye, Z.; Zhang, H.; et al., Zhou, Y. High-entropy strategy for high-temperature broadband infrared radiation and low thermal conductivity. *Ceram. Int.* **2024**, *50*, 18806-13. [DOI: 10.1016/j.ceramint.2024.02.369]

31. Kresse, G, Joubert, D. From ultrasoft pseudopotentials to the projector augmented-wave method. *Phys. Rev. B.* **1999**, *59*, 1758. [DOI:

10.1103/PhysRevB.59.1758]

32. Perdew, J P.; Burke, K, Ernzerhof, M. Generalized gradient approximation made simple. *Phys. Rev. Lett.* **1996**, *77*, 3865. [PMID: 10062328 DOI: 10.1103/PhysRevLett.77.3865]

33. Chen, G.; Min, B.; Fu, H.; et al., Near unity broadband emissivity and ultralow thermal conductivity from yttrium niobate-based ceramics. *Chem. Eng. J.* **2023**, *468*, 143695. [DOI: 10.1016/j.cej.2023.143695]

34. Liu, Q.; Cheng, H, Tu, T. Experiment and simulation of infrared emissivity properties of doped $LaAlO_3$. *J. Am. Ceram. Soc.* **2022**, *105*, 2713-24. [DOI: 10.1111/jace.18264]

35. Wang, S.; Ye, Z.; Zhang, H.; et al., High-entropy strategy for high-temperature broadband infrared radiation and low thermal conductivity. *Ceram. Int.* **2024**, *50*, 18806-13. [DOI: 10.1016/j.ceramint.2024.02.369]

36. Wang, S.; Zhang, H.; Wang, Y.; et al., Doping engineering for high-temperature broadband high emissivity and low thermal conductivity of ytterbium chromate-based ceramics. *Ceram. Int.* **2024**, *50*, 17657-64. [DOI: 10.1016/j.ceramint.2024.02.255]

37. Xia, C.; Xie, M.; Zhang, Y.; et al., High-temperature thermal conductivity and infrared emissivity of Sc_2O_3-Y_2O_3 co-stabilized ZrO_2 ceramics for thermal protective coatings. *Ceram. Int.* **2025**. [DOI: 10.1016/j.ceramint.2025.11.055]

38. Buch, A. Relations between the Elastic Moduli of Pure Metals. *Used for Evaluating the Accuracy of the Values of the Moduli.* **2001**, *43*, 452-5.

39. Shi, G.; Chen, Y.; Du, Z, Zhang, Y. Effect of Er_2O_3 and Y_2O_3 on microstructure and mechanical properties of Ti_2AlNb alloy. *J. Alloy. Compd.* **2025**, *1010*, 177169. [DOI: 10.1016/j.jallcom.2024.177169]

40. Ribeiro, T M.; Catellan, E.; Garcia, A, dos Santos, C A. The effects of Cr addition on microstructure, hardness and tensile properties of as-cast Al-3.8wt.%Cu-(Cr) alloys. *J. Mater. Res. Technol.* **2020**, *9*, 6620-31. [DOI: 10.1016/j.jmrt.2020.04.054]

41. Kim, J.; Kim, H.; Emin Kilic, M.; et al., Effect of phonon confinement on the thermal conductivity of $In_{0.53}Ga_{0.47}As$ nanofilms. *J. Appl. Phys.* **2018**, *123*, 245103. [DOI: 10.1063/1.5030178]

42. Ge, W A.; Zhao, C Y, Wang, B X. Thermal radiation and conduction in functionally graded thermal barrier coatings. Part I: Experimental study on radiative properties. *Int J. Heat. Mass. Tran.* **2019**, *134*, 101-13. [DOI: 10.1016/j.ijheatmasstransfer.2019.01.018]

43. Wang, J.; Jin, Q.; Wu, P.; et al., Unveiling the mechanisms of ultra-low thermal and oxygen-ion conductivity in entropy-stabilized ferroelastic rare-earth tantalates. *Acta. Mater.* **2025**, *283*, 120523. [DOI: 10.1016/j.actamat.2024.120523]

44. Xue, Y.; Zhao, X.; An, Y.; et al., High-entropy $(La_{0.2}Nd_{0.2}Sm_{0.2}Eu_{0.2}Gd_{0.2})_2Ce_2O_7$: A potential thermal barrier material with improved thermo-physical properties. *J. Adv. Ceram.* **2022**, *11*, 615-28. [DOI:10.1007/s40145-021-0563-1]

45. Wang, W.; Huang, R.; Zhao, Y.; et al., Adjustable zero thermal expansion in Ti alloys at cryogenic temperature. *J. Alloy. Compd.* **2018**, *740*, 47-51. [DOI: 10.1016/j.jallcom.2017.12.349]

46. Kumar, U.; Kaity, S.; Kumawat, N.; Banerjee, A, Arya, A. Thermal Expansion and Elastic Properties of Th-6U-4Zr Alloy. *T. Indian. I. Metals.* **2023**, *76*, 1751-9. [DOI: 10.1007/s12666-022-02839-4]

47. Wang, L.; Lee, B J.; Wang, X, Zhang, Z. Spatial and temporal coherence of thermal radiation in asymmetric Fabry-Perot resonance cavities. *Int. J. Heat. Mass. Tran.* **2009**, *52*, 3024-31. [DOI: 10.1016/j.ijheatmasstransfer.2009.01.042]

48. Tao, X.; Liu, J.; Xu, X.; et al., Comparative study of $MoSi_2$-borosilicate glass coatings on fibrous ceramics prepared by in-situ reaction method and two-step method. *J. Alloy. Compd.* **2016**, *684*, 488-95. [DOI: 10.1016/j.jallcom.2016.05.250]

49. Sun, L.; Marrocchelli, D, Yildiz, B. Edge dislocation slows down oxide ion diffusion in doped CeO_2 by segregation of charged defects. *Nat. Commun.* **2015**, *6*, 6294. [PMID: 25723877 DOI: 10.1038/ncomms7294]

50. Cha, J.; Zhou, C.; Lee, Y K.; Cho, S-P, Chung, I. High thermoelectric performance in n-type polycrystalline SnSe via dual incorporation of Cl and PbSe and dense nanostructures. *Acs. Appl. Mater. Inter.* **2019**, *11*, 21645-54. [PMID: 31134792 DOI: 10.1021/acsami.9b08108]

51. Flamant, Q.; Gurak, M, Clarke, D R. The effect of zirconia substitution on the high-temperature transformation of the monoclinic-prime phase in yttrium tantalate. *J.*

Eur. Ceram. Soc. **2018**, *38*, 3925-31. [DOI: 10.1016/j.jeurceramsoc.2018.04.002]

52. Jiang, B.; Lin, D-Y.; Grande, T, Selbach, S M. Local structural coupling of A-and B-site disorder in perovskite bismuth-based piezoelectrics. *Acta. Mater.* **2019**, *177*, 222-9. [DOI: 10.1016/j.actamat.2019.07.039]

53. Lewis, P M.; Keerthana, N.; Hebbar, D.; Choudhari, K, Kulkarni, S D. Cr^{3+} doped Al_2O_3 nanoparticles: Effect of Cr^{3+} content in intensifying red emission. *Curr. Appl. Phys.* **2021**, *32*, 71-7. [DOI: 10.1016/j.cap.2021.10.003]

54. Wang, Z-B.; Zhou, C-G.; Xu, H-B, Gong, S-K. Effect of thermal treatment on the grain growth of nanostructured YSZ thermal barrier coating prepared by air plasma spraying. *Chinese. J. Aeronaut.* **2004**, *17*, 119-23. [DOI: 10.1016/S1000-9361(11)60224-0]

55. Clarke, D R. Materials selection guidelines for low thermal conductivity thermal barrier coatings. *Surf. Coat. Tech.* **2003**, *163-164*, 67-74. [DOI: 10.1016/S0257-8972(02)00593-5]

56. Huang, M.; Liu, X.; Zhang, P.; et al., Thermal conductivity modeling on highly disordered crystalline $Y_{1-x}Nb_xO_{1.5+x}$: Beyond the phonon scenario. *Appl. Phys. Lett.* **2021**, *118*, [DOI: 10.1063/5.0040546]

57. Zhang, H.; Fang, W-Z.; Li, Y-M, Tao, W-Q. Experimental study of the thermal conductivity of polyurethane foams. *Appl. Therm. Eng.* **2017**, *115*, 528-38. [DOI: 10.1016/j.applthermaleng.2016.12.057]

58. Vallabh, R.; Banks-Lee, P, Mohammadi, M. Determination of Radiative Thermal Conductivity in Needlepunched Nonwovens. **2008**, *3*. [DOI: 10.1177/155892500800300406]

59. Tilioua, A.; Libessart, L, Lassue, S. Characterization of the thermal properties of fibrous insulation materials made from recycled textile fibers for building applications: Theoretical and experimental analyses. *Appl. Therm. Eng.* **2018**, *142*, 56-67. [DOI: 10.1016/j.applthermaleng.2018.06.071]

60. Schatz, J F, Simmons, G. Method of Simultaneous Measurement of Radiative and Lattice Thermal Conductivity. *J. Appl. Phys.* **1972**, *43*, 2586-94. [DOI: 10.1063/1.1661563]

61. Abeles, B. Lattice Thermal Conductivity of Disordered Semiconductor Alloys at High Temperatures. *Phys. Rev.* **1963**, *131*, 1906. [DOI: 10.1103/PhysRev.131.1906]

62. Barra-Burillo, M.; Muniain, U.; Catalano, S.; et al., Microcavity phonon polaritons from the weak to the ultrastrong phonon-photon coupling regime. *Nat. Commun.* **2021**, *12*, 6206. [PMID: 34707119 PMCID: PMC8551273 DOI: 10.1038/s41467-021-26060-x]

63. Pan, Z.; Lu, G.; Li, X.; et al., Remarkable heat conduction mediated by non-equilibrium phonon polaritons. *Nature.* **2023**, *623*, 307-12. [PMID: 37880364 DOI: 10.1038/s41586-023-06598-0]

64. Kim, S I.; Lee, K H.; Mun, H A.; et al., Dense dislocation arrays embedded in grain boundaries for high-performance bulk thermoelectrics. *Science.* **2015**, *348*. [PMID: 25838382 DOI: 10.1126/science.aaa4166]

65. Klemens, P G. Theory of lattice thermal conductivity: Role of low-frequency phonons. *Int. J. Thermophys.* **1981**, *2*, 55-62. [PMID: 31066395 DOI: 10.1039/c9cp01702j]

66. Hori, T. Role of geometry and surface roughness in reducing phonon mean free path and lattice thermal conductivity of modulated nanowires. *Int. J. Heat. Mass. Tran.* **2020**, *156*, 119818. [DOI: 10.1016/j.ijheatmasstransfer.2020.119818]

67. Chen, Z.; Zhang, X.; Lin, S.; Chen, L, Pei, Y. Rationalizing phonon dispersion for lattice thermal conductivity of solids. *Natl. Sci. Rev.* **2018**, *5*, 888-94. [DOI: 10.1093/nsr/nwy097]

68. Liu, H-Z.; Liu, Z-G.; Ouyang, J-H, Wang, Y-M. Influences of lattice vibration and electron transition on thermal emissivity of Nd^{3+} doped $LaMgAl_{11}O_{19}$ hexaaluminates for metallic thermal protection system. *Appl. Phys. Lett.* **2012**, *101*, [DOI: 10.1063/1.4759006]

69. Jiang, C-M.; Wagner, L I.; Horton, M K.; et al., Metastable Ta_2N_3 with highly tunable electrical conductivity via oxygen incorporation. *Mater. Horiz.* **2021**, *8*, 1744-55. [DOI: 10.1039/D1MH00017A]

70. Xu, X.; Xie, L.; Lou, Q.; Wu, D, He, J. Boosting the thermoelectric performance of pseudo-layered Sb_2Te_3(GeTe) *n* via vacancy engineering. *Adv. Sci.* **2018**, *5*, 1801514.

[DOI: 10.1002/advs.201801514]

71. Wang, D Z.; Liu, W D.; Li, M.; et al., Hierarchical architectural structures induce high performance in *n*-type GeTe-based thermoelectrics. *Adv. Funct. Mater.* **2023**, *33*, 2213040. [DOI: 10.1002/adfm.202213040]

72. Qian, X.; Guo, H-R.; Lyu, J-X.; et al., Enhancing thermoelectric performance of p-type SnTe through manipulating energy band structures and decreasing electronic thermal conductivity. *Rare. Metals.* **2024**, *43*, 3232-41. [DOI: 10.1007/s12598-024-02663-3]

73. Ding, S.; Kinross, A.; Wang, X.; et al., Experiment and density functional theory analyses of $GdTaO_4$ single crystal. *Solid. State. Commun.* **2018**, *273*, 5-10. [DOI: 10.1016/j.ssc.2018.02.002]

74. Yang, H.; Peng, F.; Zhang, Q.; et al., Temperature-dependent luminescence of $GdTaO_4$ single crystal. *J. Lumin.* **2015**, *160*, 90-4. [DOI: 10.1016/j.jlumin.2014.11.048]

75. Kaczkan, M.; Turczyński, S.; Pawlak, D A.; Wencka, M, Malinowski, M. Laser site-selective spectroscopy of Eu^{3+} ions doped $Y_4Al_2O_9$. *Opt. Mater.* **2016**, *58*, 412-7. [DOI: 10.1016/j.optmat.2016.06.023]

76. Abbasimofrad, S.; Almasi Kashi, M.; Noormohammadi, M, Ramazani, A. Tuning the optical properties of nanoporous anodic alumina photonic crystals by control of allowed voltage range via mixed acid concentration. *J. Phys. Chem. Solids.* **2018**, *118*, 221-31. [DOI: 10.1016/j.jpcs.2018.01.022]

77. Sun, X.; Bourham, M.; Barrett, D G.; Pal, L, McCord, M. Sustainable atmospheric-pressure plasma treatment of cellulose triacetate (CTA) films for electronics. *J. Appl. Phys.* **2020**, *128*, 075302. [DOI: 10.1063/5.0013633]

78. Lax, M, Burstein, E. Infrared Lattice Absorption in Ionic and Homopolar Crystals. *Phys. Rev.* **1955**, *97*, 39-52. [DOI: 10.1103/PhysRev.97.39]